# Anomalous spin dynamics in $CdCu_2(BO_3)_2$ revealed by $^{11}B$ NMR and ZF-$\mu$SR

W.-J. Lee,[1] S.-H. Do,[1] Sungwon Yoon,[2] Z. H. Jang,[3] B. J. Suh,[2] J. H. Lee,[4] A. P. Reyes,[5] P. L. Kuhns,[5] H. Luetkens,[6] and K.-Y. Choi[1,*]

[1]*Department of Physics, Chung-Ang University, Seoul 156-756, Republic of Korea*

[2]*Department of Physics, The Catholic University of Korea, Bucheon 420-743, Republic of Korea*

[3]*Department of Physics, Kookmin University, Seoul 136-702, Republic of Korea*

[4]*Experimental Systems Division, Rare Isotope Science Project, Institute for Basic Science, Daejeon 305-811, Republic of Korea*

[5]*National High Magnetic Field Laboratory, Florida State University, Tallahassee, Florida 32310, USA*

[6]*Laboratory for Muon Spin Spectroscopy, Paul Scherrer Institute, CH-5232 Villigen PSI, Switzerland*

(Received 11 June 2014; revised manuscript received 27 October 2014; published 4 December 2014)

We report $^{11}B$ nuclear magnetic resonance (NMR) and zero-field muon spin relaxation (ZF-$\mu$SR) measurements of the anisotropic spin tetramer system $CdCu_2(BO_3)_2$, which consists of strongly interacting Cu(1) dimers and weakly coupled nonfrustrated Cu(2) spins. Long-range magnetic order is observed at $T_N = 9.8$ K by a critical divergence of the nuclear spin-lattice relaxation rate $1/T_1$ and an appearance of well-defined muon-spin precessions. In addition, we find the spectroscopic signature for a magnetic anomaly at $T^* = 6.5$ K, a few kelvins below $T_N$. For temperatures below $T^*$, $1/T_1$ ceases to follow a $T^{4.9(1)}$ behavior. Instead, upon cooling below $T^*$, both $1/T_1$ and $1/T_2$ become temperature-independent with a subsequent small drop. The muon frequency and the relative fraction of the Cu magnetic sites show anomalies mostly for Cu(2) spins at $T^*$. This is ascribed to a Cu(2) spin reorientation. Site-specific change in magnetic structure is discussed in terms of the energy hierarchy of involved exchange interactions and an additional intertetramer interaction that controls magnetism at temperature $T^*$.

DOI: 10.1103/PhysRevB.90.214416 PACS number(s): 64.70.Tg, 76.75.+i, 75.30.Kz

## I. INTRODUCTION

Geometrical frustration has proven to be a key factor in emergent quantum phenomena and exotic states of matter, such as spin ices, magnetic monopoles, and quantum spin liquids [1]. Among frustrated spin systems, the Shastry-Sutherland lattice (SSL) occupies a special position as it is a rare example of exactly solvable spin models [2]. The SSL consists of two-dimensional arrangements of orthogonal spin dimers with intradimer coupling constant $J$ and interdimer coupling constant $J'$.

Extensive experimental and theoretical works have established a magnetic phase diagram; a ground state is tuned by the ratio $J'/J$ [3–7]. For $J'/J \leqslant 0.7$, an exact singlet state occurs, while for $J'/J \geqslant 0.7$, an antiferromagnetically (AFM) ordered phase is stabilized. With regard to materials, $SrCu_2(BO_3)_2$ is the best realization of the SSL known to date [8]. $SrCu_2(BO_3)_2$ with $J'/J \approx 0.6$–$0.64$ [9–11] is found to lie in proximity to a quantum critical point from a spin dimer side. This immediately brings to question whether a quantum phase transition can be driven to a magnetic ordered side by tuning the ratio $J'/J$. Indeed, this possibility has been thoroughly explored by tuning magnetic couplings via several different routes. It has turned out that the application of chemical or external pressure causes many-sided effects on structural and magnetic properties [12–15]. For example, external pressure induces a magnetic phase transition with no spontaneous magnetic moment [12,13], whereas chemical substitution alters a crystal structure, leading to a change of the underlying spin model [14,15]. The major impetus for the present study is to obtain a deeper understanding of the chemical pressure effects caused by replacing $Sr^{2+}$ with $Cd^{2+}$.

$CdCu_2(BO_3)_2$, which is the isovalent substitution in $SrCu_2(BO_3)_2$, has quite a different crystal structure from its mother compound due to the different ionic radii of $Sr^{2+}$ (1.32 Å) and $Cd^{2+}$ (1.09 Å) [16]. The original tetragonal ($I\bar{4}2m$) symmetry of $SrCu_2(BO_3)_2$ is lowered to the monoclinic ($P2_1/c$) symmetry for $CdCu_2(BO_3)_2$. As a consequence, $CdCu_2(BO_3)_2$ has two inequivalent Cu atoms, Cu(1) and Cu(2). As depicted in Fig. 1(a), the Cu(1) atoms form structural $Cu(1)_2O_6$ dimers within the ($\bar{1}02$) plane, similar to $SrCu_2(BO_3)_2$, while the Cu(2) atom forms tetrahedrically distorted $Cu(2)O_4$ plaquettes. The $Cu(2)O_4$ plaquettes share an oxygen atom with the $Cu(1)_2O_6$ dimers, yielding structural $Cu(1)_2Cu(2)_2O_{12}$ units with Cu ions in tetramer coordinations. The structural distortion induced by chemical substitution is expected to modify magnetic exchange interactions from the original SSL.

Using density functional theory (DFT), exact diagonalization, and quantum Monte Carlo numerical calculations, Janson *et al.* [17] derived a magnetic model of $CdCu_2(BO_3)_2$ as an anisotropic SS model. As depicted in Figs. 1(b) and 1(c), the $J_d$-$J_{t1}$-$J_{t2}$-$J_{it}$ model consists of a two-dimensional network of anisotropic magnetic tetramers with four inequivalent exchange couplings: strong intradimer coupling, $J_d$, between the Cu(1) spins and two weak intratetramer couplings, $J_{t1}$ and $J_{t2}$, between the Cu(1) and Cu(2) spins, as well as ferromagnetic intertetramer coupling, $J_{it}$, between the tetramers. The four magnetic parameters are estimated as $J_d : J_{t1} : J_{t2} : J_{it} = 1 : 0.2 : 0.45 : -0.3$ with $J_d \approx 178$ K.

Since $J_d \gg \{J_{t1}, J_{t2}, J_{it}\}$, the physics of the anisotropic SS model can be understood effectively in terms of a perturbation of the Cu(1) singlet state due to weak $\{J_{t1}, J_{t2}, J_{it}\}$ interactions. At low temperatures, the Cu(2) spins are ordered in a collinear stripe pattern by simultaneously minimizing all three $\{J_{t1}, J_{t2}, J_{it}\}$ interactions. In turn, the ordered Cu(2) moments exert local staggered fields $h_1$ and $h_2$ at the Cu(1) sites, thereby

*kchoi@cau.ac.kr

 

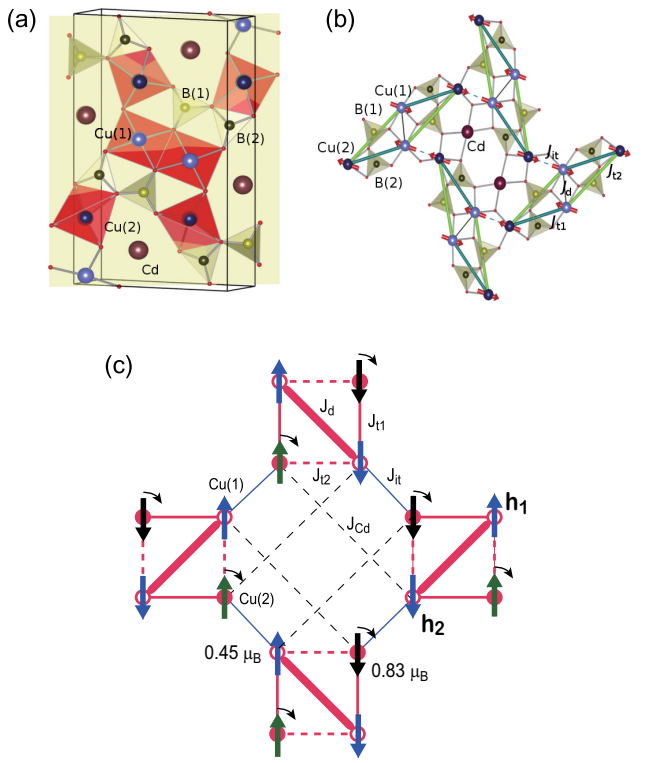


FIG. 1. (Color online) (a) Crystal structure of $CdCu_2(BO_3)_2$. The brown, light blue, dark blue, light olive, dark olive, and small red spheres denote Cd, Cu(1), Cu(2), B(1), B(2), and O ions, respectively. (b) Anisotropic spin tetramer consisting of four different exchange coupling constants: $J_d$ (black solid line), $J_{t1}$ (green bold line), $J_{t2}$ (blue bold line), and $J_{it}$ (blue dashed line) as described in the text. (c) Classical ground state of the anisotropic spin tetramer model. The black dashed line depicts the intertetramer interaction $J_{Cd}$ which couples Cu(1) and Cu(2) through Cd atoms. The blue arrows denote magnetically ordered Cu(1) spins and the black and green arrows denote magnetically ordered Cu(2) spins. The curved arrows indicate a spin reordering of Cu(2) spins which occurs upon cooling to $T^*$. $h_1$ and $h_2$ stand for local staggered fields at the Cu(1) sites. This is reproduced from Ref. [17].

polarizing the Cu(1) singlet state. The resulting ground state is schematically sketched in Fig. 1(c). Here we note that all spins point in the same direction since the collinear ordered Cu(2) spins polarize the Cu(1) spins in the same direction.

$CdCu_2(BO_3)_2$ undergoes a transition to AFM long-range ordering at $T_N = 9.8$ K [14,18]. A magnetization curve exhibits a spin-flop transition at $H_{SF} = 1.69$ T as well as a 1/2 magnetization plateau at $H_{1/2} = 23$ T [14]. A nonmagnetic-impurity study of $Cd(Cu_{1-x}Zn_x)_2(BO_3)_2$ shows a quasilinear decrease of $T_N$, $H_{SF}$, and $H_{1/2}$ with increasing Zn concentration [19]. This is consistent with dilution effects, leading to a systematic reduction of magnetic interaction energy. In contrast, the Curie-Weiss temperature varies little with $x$. This is interpreted as evidence for the disparate impact of Zn substitution on the Cu(1) and Cu(2) sites.

A neutron diffraction study has determined the magnetic structure [18]: at the Cu(1) site the magnetic moment vectors are $[0.05(5), -0.44(2), -0.04(4)]\ \mu_B$ with a magnitude of 0.45 $\mu_B$ and at the Cu(2) site they are $[-0.16(7), 0.81(2), 0.1(2)]\ \mu_B$ with a magnitude of 0.83 $\mu_B$. The ordered Cu(1) moments lie parallel to the $b$ axis while the ordered Cu(2) moments align almost along the $b$ axis, but with a small component along the directions of the $a$ and $c$ axes. The neutron results are in reasonable agreement with the prediction based on the anisotropic SS model. However, the rotation of the Cu(2) magnet moments relative to the Cu(1) ones gives a tantalizing indication of an additional control parameter for the strength and direction of Cu(2) spins, calling for further investigation. We employ site-specific local probe techniques to differentiate the evolution of magnetic moments between Cu(1) and Cu(2) sites.

In this paper we report $^{11}$B nuclear magnetic resonance (NMR) and zero-field muon spin relaxation (ZF-$\mu$SR) measurements of $CdCu_2(BO_3)_2$. The salient observation is the presence of a magnetic anomaly at $T^* = 6.5$ K, a few kelvins below $T_N$. The anomaly occurring below $T_N$ is caused by a reorientation of Cu(2) spins and demonstrates the relevance of AFM intertetramer interaction $J_{Cd}$, which was neglected in the $J_d$-$J_{t1}$-$J_{t2}$-$J_{it}$ model proposed by Janson *et al.* [17].

## II. EXPERIMENTAL DETAILS

Polycrystalline samples of $CdCu_2(BO_3)_2$ were synthesized with the conventional solid-state reaction method. Their structural and magnetic properties were characterized by x-ray diffraction and magnetization measurements as previously reported in Ref. [19].

$^{11}$B ($I = 3/2$, $\gamma_N/2\pi = 13.655$ MHz/T) NMR measurements were performed using a locally developed NMR spectrometer at National High Magnetic Field Laboratory equipped with a high-homogeneity 17 T field-varying magnet. $^{11}$B NMR spectra were recorded by integrating a spin-echo intensity while sweeping the field at a fixed frequency $\nu = 135.54$ MHz. In doing that, we employed a $\pi/2$-$\tau$-$\pi$ pulse sequence with a pulse width $\pi/2 = 4.5$ $\mu$s and a separation time $\tau = 9$ $\mu$s. The nuclear spin-lattice relaxation time, $T_1$, was measured using the saturation recovery method ($\pi/2$-$\tau_1$-$\pi/2$-$\tau_2$-$\pi$) in a temperature range of $T = 2$–200 K. The nuclear spin-spin relaxation time, $T_2$, was measured using the Hahn pulse sequence ($\pi/2$-$\tau$-$\pi$-$\tau$).

ZF-$\mu$SR measurements were performed with the GPS spectrometer at the Paul Scherrer Institute, Switzerland. A polycrystalline sample was pressed into pellets and mounted on a silver holder with a Ag foil packet. Spin-polarized positive muons were implanted into the target sample and the positron asymmetry function $a_0 P(t)$ was obtained as a function of time in a temperature range of $T = 1.5$–125 K.

## III. RESULTS

### A. $^{11}$B nuclear magnetic resonance

Figure 2(a) shows the field-swept $^{11}$B NMR spectra of $CdCu_2(BO_3)_2$ measured at a fixed frequency of $\nu = 135.54$ MHz in the temperature range of $T = 2$–200 K. At high temperatures, the $^{11}$B ($I = 3/2$) NMR powder spectra exhibit a double-peak structure with weak satellite features on either side. Since the crystal symmetry contains two inequivalent B(1) and B(2) sites [see Fig. 1(a)], the two intense peaks correspond to the central lines of the two inequivalent B

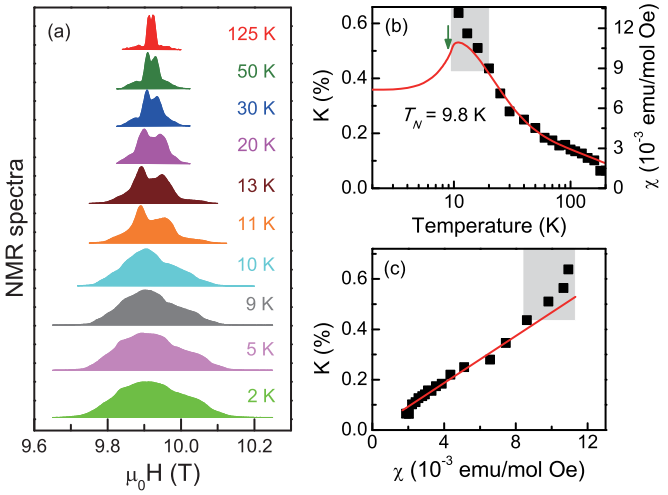


FIG. 2. (Color online) (a) Temperature dependence of the field-swept $^{11}$B NMR spectra of $CdCu_2(BO_3)_2$ obtained by integrating a spin-echo signal. (b) Temperature dependence of the magnetic shift, $K$, of $^{11}$B nuclear spins is shown together with the dc magnetic susceptibility, $\chi$, measured using a SQUID magnetometer (solid red line). (c) $K$ versus $\chi$. The red solid line is a fit to Eq. (1). The shaded rectangles indicate the deviation from a linear relation.

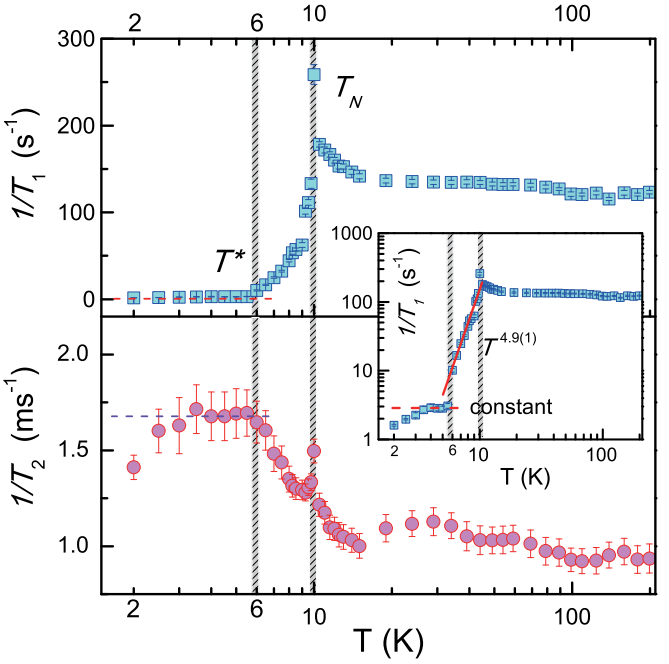


FIG. 3. (Color online) Temperature dependence of the nuclear spin-lattice relaxation rate, $1/T_1$ (upper panel), and the nuclear spin-spin relaxation rate, $1/T_2$ (lower panel), plotted in a logarithmic temperature scale. Both $1/T_1$ and $1/T_2$ show a sharp peak at $T_N$. The magnetic anomaly occurs at $T^* = 6$ K where the relaxation rates change their temperature dependence. The inset plots the temperature dependence of $1/T_1$ on a log-log scale. The solid line is a fit to a power-law behavior, $T^n$ with $n = 4.9(1)$ for $T = 6$–10 K, and the dashed lines are a guide to the eyes.

sites. As the temperature is lowered, the spectra broaden gradually with the development of a background signal. This might be related to the formation of short-range spin correlations. Furthermore, the central peaks move away from each other. For temperatures below $T_N$, the NMR spectrum is made of a dozen peaks which overlap with each other due to four-sublattice magnetic structure with site-dependent magnetic moments. The complex spectrum does not allow for extraction of concrete information about spin structure and internal magnetic field (order parameter). If single crystals could be grown, the spin structure could be conclusively resolved.

In Fig. 2(b) the temperature dependence of the magnetic shift, $K$, is plotted with the dc magnetic susceptibility measured at $H = 2$ kOe. Here $K$ is determined by taking the middle point of the two central peaks. We note that the magnetic shift cannot be resolved for temperatures below $T_N$ due to the broadened spectral shape. The magnetic shift is a direct measure of intrinsic spin susceptibility. By correlating the magnetic shift with the static susceptibility, we can extract the hyperfine interaction ($A_{hf}$) between the $^{11}$B nuclear and $Cu^{2+}$ electronic spins from the Clogston-Jaccarino plot [20]. Using the relation shown in Fig. 2(c), the hyperfine interaction can be directly determined from the slope through

$$K(T) = K_{\text{chem}} + \frac{A_{hf}}{N_A}\chi_{\text{spin}}(T). \qquad (1)$$

The first term, $K_{\text{chem}}$, is a temperature-independent chemical or orbital shift and $N_A$ is the Avogadro number. The $K$-$\chi$ plot is fitted well by a straight line in a wide temperature range of $T = 25$–200 K. In this respective temperature range, we obtain the hyperfine coupling constant, $A_{hf} \approx 0.047(5)$ T/$\mu_B$, and $K_{\text{chem}} \approx -0.0037$ T/$\mu_B$. As the temperature is lowered from 25 K toward $T_N$, deviation from the linear relation as indicated by the shaded rectangles in Fig. 2(c) is observed. This might be because short-range-ordered $Cu^{2+}$ moments contribute to $A_{hf}$.

Relaxation measurements were performed to study the evolution of magnetic correlations. Figure 3 exhibits the temperature dependence of the nuclear spin-lattice relaxation rate, $1/T_1$, in a logarithmic temperature scale along with $1/T_2$. $1/T_1$ is nearly constant for temperatures above $T = 20$ K. The temperature-independent $1/T_1$ behavior is typical for fast-fluctuating paramagnets in the high-temperature limit. As the temperature is lowered from $T = 20$ K, $1/T_1$ increases rapidly and then exhibits a sharp peak around $T_N$, confirming long-range magnetic ordering. In the AFM-ordered state, $1/T_1$ is normally governed by the scattering of magnons off nuclear spins. For $T \gg \Delta$ where $\Delta$ is the magnon gap, $1/T_1$ follows either a $T^3$ behavior due to a two-magnon Raman process or a $T^5$ behavior due to a three-magnon process [21,22]. For $T \ll \Delta$, the spin-lattice relaxation rate is given by an activated behavior $1/T_1 \propto T^2 \exp(-\Delta/T)$. As seen from the log-log plot of $1/T_1$ in the inset of Fig. 3, our $1/T_1$ data in the temperature range of $T = 6$–10 K are approximated by a $T^5$ behavior, $1/T_1 \sim T^{4.9(1)}$. This suggests that the relaxation is dominated by the three-magnon Raman process. The $T^5$ behavior is characteristic of a canted antiferromagnet having an isotropic hyperfine interaction [23]. As $T \to 0$ K, however, the anticipated activation behavior is lacking (not shown here). Instead, $1/T_1$ flattens out with a subsequent small drop

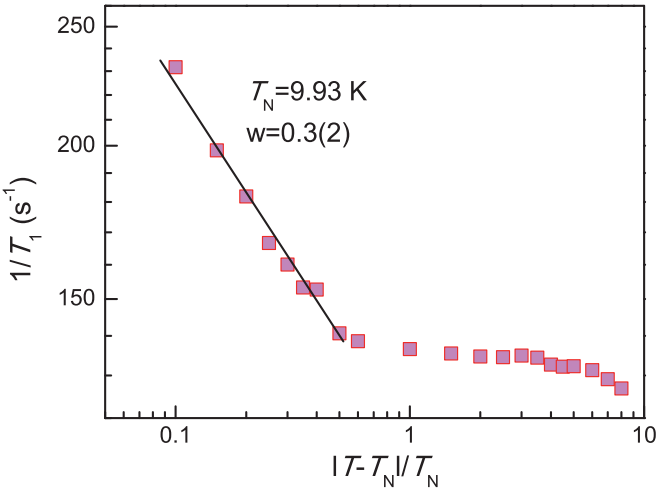


FIG. 4. (Color online) $1/T_1$ versus reduced temperature $|T - T_N|/T_N$ on a log-log scale. The solid line is a fit to the relation $1/T_1 \propto (T/T_N - 1)^{-w}$ with $w = 0.3(2)$ and $T_N = 9.93$ K.

for temperatures below 6 K. This is not consistent with a conventional magnet, suggesting the presence of a magnetic anomaly.

We turn to the temperature dependence of the nuclear spin-spin relaxation rate, $1/T_2$. Although $1/T_2$ contains extrinsic effects, for example, domain motion and spin diffusion, it can provide complementary information to $1/T_1$. $1/T_2$ is largely $T$-independent for $T > 20$ K. As the temperature is decreased from 20 K to 6 K, $1/T_2$ increases with a weak but discernible peak at $T_N$. For temperatures below 6 K, $1/T_2$ becomes constant with a subsequent small drop. Overall, the $T$-dependent behaviors of $1/T_1$ and $1/T_2$ in the ordered state are alike, which ascertains the intrinsic nature of the magnetic anomaly at $T^* = 6$ K. At the respective temperature, no discernible anomaly has been reported in specific heat and Bragg peak intensities [18]. This means that the anomaly involves a tiny reorientation of part of the spins (see below).

The divergence of the spin-lattice relaxation rate is a signature of a second-order phase transition to AFM ordering. To analyze critical phenomena, we plot $1/T_1$ vs reduced temperature $|T - T_N|/T_N$ on a log-log scale in Fig. 4. In the narrow temperature region of $|T - T_N|/T_N \leqslant 0.5$, the critical relaxation rate is well described by $1/T_1 \propto (T/T_N - 1)^{-w}$ where $w$ is the critical exponent. By fixing the transition temperature to $T_N = 9.93$ K, the critical exponent is estimated to be $w = 0.3(2)$. For a three-dimensional isotropic Heisenberg antiferromagnet, a mean field theory predicts $w = 1/2$ and a dynamic scaling theory gives $w = 1/3$ [24,25]. Our value is close to the latter $w = 1/3$, confirming that the critical relaxation rate is given by three-dimensional fluctuations of local antiferromagnetic moments.

### B. Muon spin relaxation

We further employed the $\mu$SR technique to investigate a magnetic order parameter and spin relaxation rate. The experiments were carried out with the $\pi$M3 beam line at the Paul Scherrer Institute (Villigen, Switzerland). The data were analyzed using the free software package MUSRFIT [26]. Figure 5

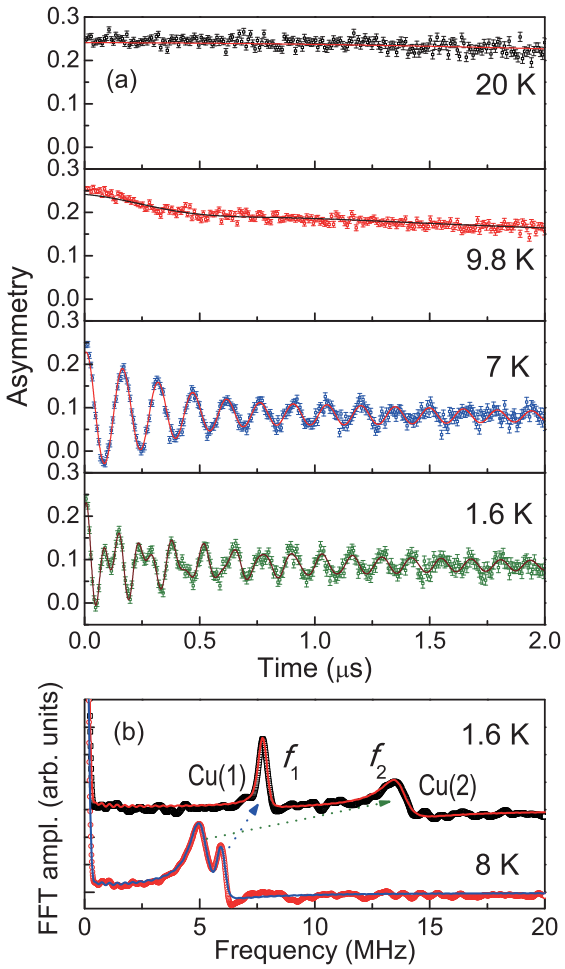


FIG. 5. (Color online) (a) Temperature dependence of the ZF-$\mu$SR spectra of $CdCu_2(BO_3)_2$ in a temperature range of $T = 1.6$–20 K. (b) Representative Fourier amplitude spectra at $T = 1.6$ and 8 K. The solid lines are fits to Eq. (2), as described in the text. $f_1$ and $f_2$ are assigned to local fields arising from the Cu(1) and the Cu(2) site, respectively.

shows the representative ZF-$\mu$SR spectra of $CdCu_2(BO_3)_2$ at various temperatures. At $T = 20$ K we observe the slow Gaussian damping expected for muon relaxations due to random local magnetic fields from nuclear magnetic moments (mainly from $^{63}$Cu, $^{65}$Cu, and $^{11}$B). In the paramagnetic phase, the spectra are well described by the Kubo-Toyabe relaxation function $G^{KT}(\Delta,t)$ with a linewidth $\Delta = 0.18(5)$ MHz determined by the nuclear dipolar fields [27]. The absence of additional exponential relaxation indicates that electron spin fluctuations are too fast in a $\mu$SR time window. This is consistent with the $T$-independent behavior of both $1/T_1$ and $1/T_2$ above 20 K (see Fig. 3). For temperatures below $T_N$, we observe well-defined muon-spin precession signals, confirming the occurrence of a long-range AFM order. The Fourier transform of the ZF-$\mu$SR spectrum at $T = 1.6$ K clearly shows the two frequencies at $f_1 = 7.7(7)$ and $f_2 = 13.7(3)$ MHz [see Fig. 5(b)]. For oxide compounds, muons bind to $O^{2-}$ ions with a bond length of $\sim$1 Å [28,29]. The muons can reside near an apical $O^{2-}$ of each Cu(1) and Cu(2) site. Based on the observed two frequencies, we conclude that

the two muon stopping sites are identical. Therefore, the two frequencies correspond to local dipolar fields arising from the two magnetically different Cu(1) and Cu(2) sites (see below).

Noticeably, the ZF spectrum at $T = 1.6$ K consists of a constant background and a rapidly damped oscillating component. The 1/3 tail is what is expected for a powder sample in an ordered state [30]. The rapid damping suggests the formation of a static but inhomogeneous internal field at the muon sites. Taking into account these observations, the ZF-$\mu$SR spectra are analyzed using the sum of an exponentially relaxing cosine oscillation for the static internal fields and exponentially relaxing nonoscillatory signals for dynamic fluctuating moments:

$$P(t) = \sum_{j=1}^{2} A_j[\alpha_j \cos(2\pi f_j t + \phi_i)\exp(-\lambda_{Tj}t) + (1-\alpha_j)\exp(-\lambda_{Lj}t)]. \quad (2)$$

Here $A_j$ is the relative volume fraction of the two different Cu(1) and Cu(2) sites. $f_j$ is the muon Larmor frequency corresponding to the static internal AFM field and $\phi_j$ is the initial phase of the oscillatory signal and is constant over the whole temperature range. $\lambda_{T_j}$ and $\lambda_{L_j}$ are the respective transverse and longitudinal relaxation rates. As evident from Fig. 5, the adopted model reproduces the experimental spectra quite well. We further note that the inclusion of the Kubo-Toyabe relaxation function, $G^{KT}(\Delta,t)$, in the ordered state gives a negligible value of $\Delta \approx 0$ MHz.

In Fig. 6 we plot the temperature dependence of the muon spin precession frequencies, $f_j$, the transverse relaxation rates, $\lambda_{T_j}$, the longitudinal relaxation rates, $\lambda_{L_j}$, and the normalized fraction of the two magnetic sites, $A_i/(A_1 + A_2)$. The ratio of the two muon frequencies at $T = 1.6$ K is calculated to be 1 : 1.962. This is very close to the ratio of the Cu(1) to the Cu(2) ordered moment: $\langle S_{\mathrm{Cu}(1)}\rangle : \langle S_{\mathrm{Cu}(2)}\rangle = 0.45\ \mu_B : 0.83\ \mu_B = 1 : 1.844$ [18]. This corroborates that the two frequencies result from the two different Cu moments and allows the assignment of the frequencies $f_1$ and $f_2$ to the respective Cu(1) and the Cu(2) site.

The temperature dependence of $f_j$ is fitted to the expression

$$f_j(T) = f_j(0)[1 - (T/T_N)]^{\beta}, \quad (3)$$

where $f_j(0)$ denotes the initial frequency at $T = 0$ and $\beta$ is the critical exponent. The extracted value of $\beta$ varies with the choice of $T_N$. With a view of obtaining the reliable critical exponent, we check the goodness of fit for various choices of $T_N$ for a fixed range of frequencies, $f_j(T) \in [0,5]$ MHz [31]. Choosing $T_N < 9.66$ K is not justified because the muon precessions start to appear at $T = 9.66$ K. For values of $T_N > 9.72$ K, a critical behavior is no longer visible over a wide temperature range. The goodness of fit, $X_j^2 = \sum_i [f_j^{\mathrm{cal}}(\tau_i) - f_j^{\mathrm{exp}}(\tau_i)]^2$ $(j = 1,2)$ with $\tau_i = T_i/T_N - 1$, is shown in the upper inset of Fig. 7 as a function of $T_N \in [9.66,9.72]$ K. The corresponding variation of the critical exponent $\beta$ is displayed together. A minimum in $X_j^2$ is seen at $T_N = 9.68$ K [here shown only for the Cu(1) spins]. The best fit obtained for $T_N = 9.68$ K yields a value of $\beta = 0.36(8)$ for the Cu(1) site and $\beta = 0.39(4)$ for the Cu(2) site. The goodness of the fit for fixed $T_N$ saturates for $\tau_i < 0.15$ (see the lower inset of Fig. 7).

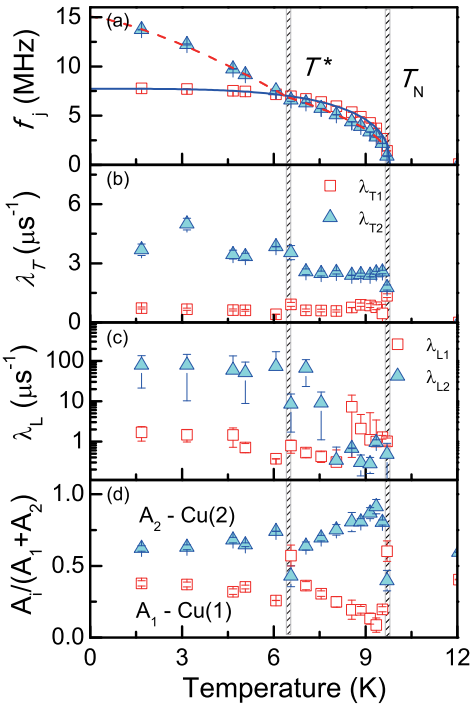


FIG. 6. (Color online) (a) Temperature dependence of muon spin frequencies $f_j$. The solid and dashed lines are a guide to the eyes. (b) Temperature dependence of transverse relaxation rates, $\lambda_{T_j}$. (c) Temperature dependence of longitudinal relaxation rates, $\lambda_{L_j}$. (d) Normalized fraction of two magnetic sites, $A_i/(A_1 + A_2)$. The vertical bars denote the magnetic ordering at $T_N$ and the magnetic anomaly at $T^*$. The tatched bars indicate $T_N$ and $T^*$.

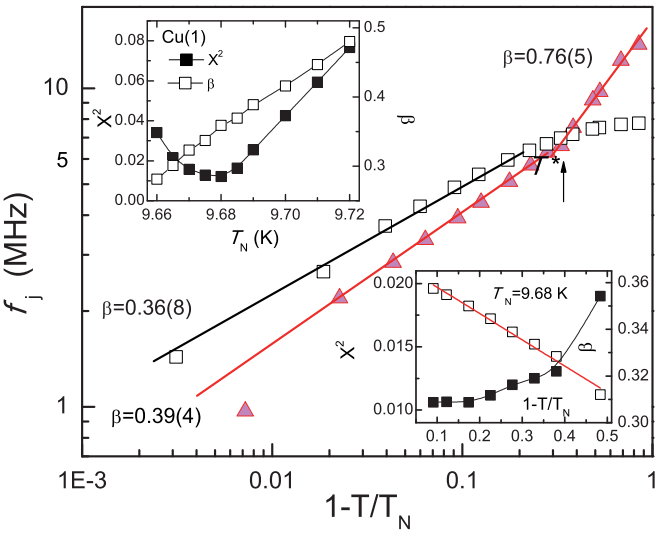


FIG. 7. (Color online) A log-log plot of muon spin frequencies $f_j$ vs reduced temperature $1 - T/T_N$ for the chosen best value of $T_N = 9.68$ K. The solid lines are fits to Eq. (3). The upper inset shows the goodness of fit parameters, $X^2$ (full squares), and the corresponding exponent $\beta$ (open squares) vs the chosen value for $T_N$. The lower inset shows $X^2$ and $\beta$ vs reduced temperature for fixed $T_N = 9.68$ K.

A conservative estimate gives $T_N \in [9.67,9.69]$ K, yielding $\beta \in [0.32,0.39]$ for the Cu(1) moment and $\beta \in [0.37,0.42]$ for the Cu(2) moment.

Figure 7 shows a log-log plot of $f_j(T)$ vs the reduced temperature, $1 - T/T_N$, with the chosen best value of $T_N = 9.68$ K. The critical exponent of the Cu(1) [Cu(2)] site is close to (larger than) $\beta = 0.367$, which is known for a 3D Heisenberg antiferromagnet [32].

Lastly, we inspect the $\mu$SR parameters to examine the magnetic anomaly. We observe small but discernible anomalies at about $T^* = 6.5$ K. This temperature is a little higher than the one from the NMR results. The small discrepancy is due to the absence/presence of an external field in NMR and $\mu$SR measurements. Several noteworthy features emerge, as follows.

First, $f_2(T)$ increases substantially below $T^*$, which is described by $\beta = 0.76(5)$ (see Fig. 7). This value should not be taken as the critical exponent since the anomaly at $T^*$ is not a thermodynamic phase transition. This anomaly is absent for $f_1(T)$. Second, with decreasing temperature from $T_N$, $\lambda_{L_2}$ increases steeply and then becomes constant for temperatures of $T < T^*$. This is contrasted by near complete lack of change of $\lambda_{L_1}$ when crossing temperature $T^*$. Third, $A_1/(A_1 + A_2)$ $[A_2/(A_1 + A_2)]$ increases (decreases) monotonically with lowering temperature to $T^*$ and then becomes constant for $T < T^*$. These features indicate that the Cu(2) spins are mostly susceptible to the magnetic anomaly at $T^*$, while the Cu(1) spins remain nearly intact. The lack of anomaly in the specific heat and intensity of the magnetic reflection at (0,0,1) suggests that the $T^*$ anomaly does not involve a large entropy change. Rather, it is driven by a tiny reorientation of the Cu(2) spins. We stress that the site-specific anomaly is not compatible to extrinsic effects such as glassy behavior due to impurities.

## IV. DISCUSSION

Having established that the Cu(2) spin reordering acts as the primary cause of the $T^*$ magnetic anomaly, we will discuss its origin. Before proceeding, we will recapitulate the peculiar spin topology of $CdCu_2(BO_3)_2$, which is sketched in Fig. 1(c).

The energy hierarchy of exchange coupling constants allows decomposition of the anisotropic SSL into two subsystems: (i) strongly coupled Cu(1) dimers by $J_d \sim 178$ K (denoted by the thick line) and (ii) nonfrustrated, weakly coupled Cu(2) spins by $\{J_{t1}, J_{t2}, J_{it}\} \ll J_d$ (denoted by the thin lines). In this case, the magnetism of $CdCu_2(BO_3)_2$ is approximated by a perturbation of the Cu(1) singlet state by the weak $\{J_{t1}, J_{t2}, J_{it}\}$ interactions. In the high-temperature limit, the Cu(1) spins tend to form spin singlets while the Cu(2) spins are disordered. At low temperatures, the nonfrustrated interactions of $J_{t1}$, $J_{t2}$, and $J_{it}$ between the Cu(2) spins become a relevant energy scale and thereby induce collinear stripe ordering. In turn, the staggered fields $h_1$ and $h_2$ produced by the ordered Cu(2) moments polarize the Cu(1) singlet state in a staggered pattern. In this perturbation description, the magnetic ordering mechanism differs entirely between the two subsystems: the Cu(2) spin ordering by magnetic interactions and the Cu(1) spin ordering by polarization. This provides a natural explanation for why the Cu(2) ordered magnetic moment is much larger than the Cu(1) one, as well as why the fraction of the Cu(1) magnetic sites increases against that of the Cu(2) sites as the temperature is lowered from $T_N$ to $T^*$ [see Fig. 6(d)].

In spite of the success of the $J_d$-$J_{t1}$-$J_{t2}$-$J_{it}$ model in capturing the above-mentioned experimental results, it fails to reproduce the small rotation of the Cu(2) magnet moments relative to the Cu(1) ones observed by the neutron diffraction [17,18] and the Cu(2) spin reordering seen by $\mu$SR. Within this minimal model the Cu(1) and Cu(2) spins are expected to align in the same direction [see the arrows in Fig. 1(c)]. This calls for a mechanism which accounts for a tilting of the Cu(2) spins from the $b$ axis. The magnetic structure can be altered by either temperature-induced modification of magnetic interactions or additional magnetic interaction. The former mechanism is improbable because there is no hint of lattice distortion at the respective temperatures [18]. The remaining mechanism that can drive the spin reordering is additional intertetramer interaction, particularly in the form of AFM interaction. It is clear that such an AFM intertetramer changes the ordering pattern at the Cu(2) site and strengthens AFM ordering as seen from the steep increase of $f_2$ in Fig. 7. Indeed, the DFT calculations by Janson *et al.* [17] showed the presence of another intertetramer exchange interaction, $J_{\mathrm{Cd}}$, which couples the Cu(1) and the Cu(2) spins via Cd atoms [see the thin dashed lines in Fig. 1(c)]. In formulating the minimal $J_d$-$J_{t1}$-$J_{t2}$-$J_{it}$ model, this term, $J_{\mathrm{Cd}} \sim 5$ K, was ignored due to its small size. Of particular note, $J_{\mathrm{Cd}}$ and $T^*$ are pretty much the same energy, evidencing their relevance to magnetism.

We consider how the inclusion of $J_{\mathrm{Cd}}$ affects the magnetic structure. Because of the large energy difference between Cu(1) and Cu(2) subsystems, $J_{\mathrm{Cd}}$ primarily involves the Cu(2) subsystem. When $J_{\mathrm{Cd}}$ is introduced, the Cu(1) and Cu(2) spins in the different tetramers are coupled. This competes with the FM intertetramer interaction $J_{it}$, thereby inducing a slight rotation of the Cu(2) spins from the collinear stripe ordering structure, which was calculated in the absence of $J_{\mathrm{Cd}}$ [17]. This is sketched by the curved arrows in Fig. 1(c). The remaining question is how the Cu(1) spin orientation is retained while that of Cu(2) is not. The staggered fields $h_1$ and $h_2$ at the Cu(1) spins are determined by the direction and magnitude of the Cu(2) ordered magnetic moments. The addition of $J_{\mathrm{Cd}}$ increases an exchange energy of the Cu(2) spins and thus the corresponding exchange fields become stronger. At the same time, the Cu(2) magnetic moments are tilted away from the direction parallel to the Cu(1) ones. As a result, the increase of the exchange fields at the Cu(1) sites are nullified. Thus, the effective staggered fields $h_1$ and $h_2$ barely change.

## V. CONCLUSION

We have presented combined $^{11}$B NMR and ZF-$\mu$SR measurements of the anisotropic spin tetramer system $CdCu_2(BO_3)_2$. We observe the spectroscopic signature for long-range magnetic ordering at $T_N = 9.8$ K as a critical divergence of $1/T_1$ and an appearance of well-defined muon-spin precessions. The major finding is the presence of a magnetic anomaly at $T^* = 6.5$ K in the ordered phase. This is

evidenced by discernible anomalies in NMR relaxation rates as well as in muon frequencies and a relative fraction of the Cu magnetic sites below $T^*$. This is ascribed to Cu(2) spin reordering. As its underlying mechanism, we discuss the energy hierarchy of the anisotropic spin tetramer system, constituting the strongly interacting Cu(1) dimers and the weakly coupled nonfrustrated Cu(2) spins. A large difference of the involved energies between the two subunits allows the Cu(2) spins to be treated separately from the Cu(1) ones at low temperatures. In this peculiar spin topology, the addition of the AFM intertetramer interaction, $J_{Cd}$, affects the Cu(2) spin sector exclusively. A site-specific control of magnetic structure is a unique feature of the spin tetramer system, which is anisotropic in magnetic exchange interactions.

## ACKNOWLEDGMENTS

We would like to thank H. H. Klauß and H. Maeter for their constructive input and assistance with $\mu$SR measurements. This work was supported by Korea NRF Grants No. 2012-046138 and No. 2012M7A1A2055645. A portion of this work was performed at the National High Magnetic Field Laboratory, which is supported by NSF Cooperative Agreement No. DMR-0654118, and by the State of Florida.

[1] L. Balents, Nature (London) **464**, 199 (2010).
[2] B. C. Shastry and B. Sutherland, Physica B **108**, 1069 (1981).
[3] See for a review S. Miyahara and K. Ueda, J. Phys.: Condens. Matter **15**, R327 (2003).
[4] H. Kageyama, *Frontiers in Magnetic Materials* (Springer, Berlin, 2005), p. 611.
[5] M. E. Zayed, Ch. Ruegg, Th. Strassle, U. Stuhr, B. Roessli, M. Ay, J. Mesot, P. Link, E. Pomjakushina, M. Stingaciu, K. Conder, and H. M. Rønnow, Phys. Rev. Lett. **113**, 067201 (2014).
[6] P. Corboz and F. Mila, Phys. Rev. Lett. **112**, 147203 (2014).
[7] Y. H. Matsuda, N. Abe, S. Takeyama, H. Kageyama, P. Corboz, A. Honecker, S. R. Manmana, G. R. Foltin, K. P. Schmidt, and F. Mila, Phys. Rev. Lett. **111**, 137204 (2013).
[8] H. Kageyama, K. Yoshimura, R. Stern, N. V. Mushnikov, K. Onizuka, M. Kato, K. Kosuge, C. P. Slichter, T. Goto, and Y. Ueda, Phys. Rev. Lett. **82**, 3168 (1999).
[9] S. Miyahara and K. Ueda, J. Phys. Soc. Jpn. **69** (Suppl. B), 72 (2000).
[10] A. Koga and N. Kawakami, Phys. Rev. Lett. **84**, 4461 (2000).
[11] C. Knetter, A. Bühler, E. Müller-Hartmann, and G. S. Uhrig, Phys. Rev. Lett. **85**, 3958 (2000).
[12] T. Waki, K. Arai, M. Takigawa, Y. Saiga, Y. Uwatoko, H. Kageyama, and Y. Ueda, J. Phys. Soc. Jpn. **76**, 073710 (2007).
[13] M. Takigawa, T. Waki, M. Horvatic, and C. Berthier, J. Phys. Soc. Jpn. **79**, 011005 (2010).
[14] M. Hase, M. Kohno, H. Kitazawa, O. Suzuki, K. Ozawa, G. Kido, M. Imai, and X. Hu, Phys. Rev. B **72**, 172412 (2005).
[15] S. Mitsudo, M. Yamagishi, T. Fujita, Y. Fujimoto, M. Toda, T. Idehara, and M. Hase, J. Magn. Magn. Mater. **310**, e418 (2007).
[16] R. D. Shannon, Acta Cryst. A **32**, 751 (1976).
[17] O. Janson, I. Rousochatzakis, A. A. Tsirlin, J. Richter, Y. Skourski, and H. Rosner, Phys. Rev. B **85**, 064404 (2012).
[18] M. Hase, A. Dönni, V. Y. Pomjakushin, L. Keller, F. Gozzo, A. Cervellino, and M. Kohno, Phys. Rev. B **80**, 104405 (2009).
[19] S. H. Do, J. W. Hwang, K.-Y. Choi, H. Zhou, and H. Nojiri, J. Kor. Phys. Soc. **63**, 1028 (2013).
[20] R. Nath, Y. Furukawa, F. Borsa, E. E. Kaul, M. Baenitz, C. Geibel, and D. C. Johnston, Phys. Rev. B **80**, 214430 (2009).
[21] D. Beeman and P. Pincus, Phys. Rev. **166**, 359 (1968).
[22] M. Belesi, F. Borsa, and A. K. Powell, Phys. Rev. B **74**, 184408 (2006).
[23] R. J. Mahler, A. C. Daniel, and P. T. Parrish, Phys. Rev. Lett. **19**, 85 (1967).
[24] T. Moriya and K. Ueda, Solid State Commun. **15**, 169 (1974).
[25] H. Benner and J. P. Boucher, in *Magnetic Properties of Layered Transition Metal Compounds*, edited by L. J. de Jongh (Kluwer Academic Publishers, Dordrecht, 1990).
[26] A. Suter and B. M. Wojek, Phys. Procedia **30**, 69 (2012).
[27] R. S. Hayano, Y. J. Uemura, J. Imazato, N. Nishida, T. Yamazaki, and R. Kubo, Phys. Rev. B **20**, 850 (1979).
[28] E. Holzschuh, A. B. Denison, W. Kundig, P. F. Meier, and B. D. Patterson, Phys. Rev. B **27**, 5294 (1983).
[29] S. R. Dunsiger, A. A. Aczel, C. Arguello, H. Dabkowska, A. Dabkowski, M.-H. Du, T. Goko, B. Javanparast, T. Lin, F. L. Ning, H. M. L. Noad, D. J. Singh, T. J. Williams, Y. J. Uemura, M. J. P. Gingras, and G. M. Luke, Phys. Rev. Lett. **107**, 207207 (2011).
[30] A. Yaouanc and P. Dalams de Reotier, *Muon Spin Rotation, Relaxation, and Resonance* (Oxford University Press, Oxford, 2011).
[31] M. J. P. Gingras, C. V. Stager, N. P. Raju, B. D. Gaulin, and J. E. Greedan, Phys. Rev. Lett. **78**, 947 (1997).
[32] C. Holm and W. Janke, Phys. Rev. B **48**, 936 (1993).